AGU PUBLICATIONS

JGR

Journal of Geophysical Research: Solid Earth

RESEARCH ARTICLE
10.1002/2016JB013809

Key Points:
- Demonstrates effective use of microearthquakes for reflection imaging with dense seismic arrays and seismic interferometry
- Reflections from an interface at the same depth as magma encountered in boreholes at Krafla, Iceland
- Method is applicable to a wide range of geologic and energy problems which involves natural or induced seismicity

Correspondence to:
D. Kim,
dk696@cornell.edu

Citation:
Kim, D., L. D. Brown, K. Árnason, K. Águstsson, and H. Blanck (2017), Magma reflection imaging in Krafla, Iceland, using microearthquake sources, *J. Geophys. Res. Solid Earth*, *122*, 5228–5242, doi:10.1002/2016JB013809.

Received 29 NOV 2016
Accepted 18 JUN 2017
Accepted article online 21 JUN 2017
Published online 11 JUL 2017

Magma reflection imaging in Krafla, Iceland, using microearthquake sources

Doyeon Kim[1], Larry D. Brown[1], Knútur Árnason[2], Kristján Águstsson[2], and Hanna Blanck[2]

[1]Earth and Atmospheric Sciences, Cornell University, Ithaca, New York, USA, [2]Iceland Geosurvey (ISOR), Reykjavik, Iceland

Abstract The details of magma plumbing beneath active volcanoes remain a major challenge in geochemistry, geophysics, and volcanic hazard evaluation. Here we apply a relatively novel variation of seismic interferometry, which we call Virtual Reflection Seismic Profiling, to produce a high-resolution image of a known crustal magma body. The technique takes advantage of recent advances in both seismic instrumentation (dense arrays) and seismic analysis (seismic interferometry). We have applied this technique to data recently acquired at an iconic volcanic system, Krafla, which lies on the mid-Atlantic ridge as exposed in northern Iceland. What make this particular site exceptional are encounters with rhyolitic magma in two drill holes, K-39 and Iceland Deep Drilling Project-1 (IDDP-1). These known magma bodies represent a unique calibration opportunity for surface geophysical measurements of magma distribution at depth. In this study, we produced a stacked, seismic reflection section by applying common depth point processing techniques to virtual shot gathers derived from interferometry of *P* waves from microearthquakes generated by tectonic, magmatic, and/or geothermal activity. We observe a strong, coherent reflection on the seismic section at a travel time corresponding to the depth at which magma was encountered in the IDDP-1 wellbore. We interpret this reflection to be from magma or magma-related fluids. Additional coherent reflections may correspond to other components of the magma plumbing beneath Krafla. These results represent a promising new technique for structural imaging with natural sources that can be applied to a wide array of geologic and energy problems that involve natural or induced seismic clusters.

1. Introduction

The distribution and movement of magma in the earth's crust have been a critical concern of geochemical and geophysical investigations for much of the past century [e.g., *Spera*, 1980; *Crisp*, 1984; *Corry*, 1988; *Glazner and Ussler*, 1988; *Emerman and Marrett*, 1990; *Ishihara*, 1990; *Parsons et al.*, 1992; *Gudmundsson*, 2000; *Polteau et al.*, 2008]. Fundamental and persistent questions related to magma plumbing include the relative importance of magma chambers versus sill or dyke complexes, the role of density and viscosity in the transport of magma in the crust, the relative mixing of original magma with host rocks during ascent, and ultimately, the recognition of precursors to major eruptive events [e.g., *Voight and Cornelius*, 1991; *Scarpa*, 2001].

Some of the better known attempts at magma imaging with seismic methods include passive tomographic studies [*Lees*, 2007] to delineate the magma chambers beneath Yellowstone [e.g., *Iyer et al.*, 1981; *Benz and Smith*, 1984; *Huang et al.*, 2015], efforts to map the Socorro magma body under central New Mexico using reflected body waves from microearthquake sources [e.g., *Sanford and Long*, 1965; *Sanford et al.*, 1973; *Sanford et al.*, 1977], and similar work in Japan to associate magma with reflected shear waves on microearthquake recordings [e.g., *Matsumoto and Hasegawa*, 1996]. There are also now a number of examples of magma bodies being detected and/or mapped by multichannel controlled-source surveys, beginning with COCORP's profiling of the Socorro Magma Body in 1976 [*Brown et al.*, 1979; *Brocher*, 1981] and detection of a similar sill-like body beneath Death Valley [*De Voogd et al.*, 1986]. Another prominent example of magma bodies being mapped by surface reflection surveys are the INDEPTH surveys on the southern Tibetan Plateau [*Brown et al.*, 1996; *Makovsky et al.*, 1999], which have been cited to support the role of partial melting in plateau uplift [*Nelson et al.*, 1996]. Active seismic reflection mapping of magma chambers, including 3-D, has been achieved beneath mid-ocean ridges by marine multichannel profiling [e.g., *Mutter et al.*, 1988; *Kent et al.*, 2000]. New passive techniques, such as receiver functions, have also reported the presence of molten material at intracrustal depths, including independent detection of the Socorro Magma Body [*Sheetz and Schlue*, 1992] and perhaps most notably the mapping of the Altiplano-Puna magma body

beneath the central Andes [*Zandt et al.*, 2003; *Ward et al.*, 2014]. In many cases, the interpretation of magma from the seismic results has been strongly bolstered by complementary geophysical measurements, most notably magnetotelluric [e.g., *Wei et al.*, 2001].

The aforementioned diverse seismological results represent independent but complementary means of detecting magma at crustal depths, each with its strengths and limitations. For example, receiver functions can probe to sublithospheric depths, but the bandwidth typically available from teleseismic sources severely limits resolution within the crust [*Cassidy*, 1992] and attenuation/scattering in volcanic areas often hampers the penetration achievable with higher-resolution active surface seismic surveys [e.g., *Ziolkowski et al.*, 2003]. Moreover, the source costs associated with conventional multichannel seismic reflection surveys on land is often prohibitive, especially in rugged terrain.

Subsurface imaging by processing the ambient noise field with a technique known as seismic interferometry has become a widely used and powerful tool for crustal-scale velocity imaging using surface wave tomography [e.g., *Shapiro et al.*, 2005; *Lin et al.*, 2008]. However, the effectiveness of interferometry in extracting useful body wave information from ambient noise has been more challenging. *Roux et al.* [2005] documented the presence of *P* waves in their analysis of ambient noise in southern California. *Draganov et al.* [2009, 2013] describes efforts related to oil and gas exploration, while *Ryberg* [2011] reports recovery of both wide-angle reflections and refractions that correlate with their counterparts from explosive sources in a regional seismic survey. *Yu and Schuster* [2001] use seismic noise generated by drilling operation to recover the reflectivity distribution beneath the survey. At a larger scale, seismic interferometry of ambient noise has been used to recover Moho reflections [e.g., *Tibuleac and von Seggern*, 2012; *Gorbatov et al.*, 2013], reflections form the lithosphere-asthenosphere boundary [*Kennett*, 2015], and prominent core phases [*Lin et al.*, 2013a]. Although most interferometric analyses of both surface and body waves attempt to extract useful information from unknown, presumably random noise sources, of particular relevance to this study is the use of selected known sources. This application of interferometry has found numerous applications in the exploration industry [e.g., *Wapenaar et al.*, 2008; *Schuster*, 2009] and has recently found application to earthquake sources. For example, *Ruigrok and Waapenaar* [2012] used interferometry of global phases from appropriately located teleseismic events to image lithospheric structure beneath southern Tibet. *Nakata et al.* [2014] retrieved body waves in southwestern Wyoming using multidimensional deconvolution of recordings of local and regional earthquakes. *Nishitsuji et al.* [2016] has produced crustal-scale reflection imagery using interferometry of the *P* coda from regional earthquakes in the southern Andes. Here we apply a similar approach to high-resolution imaging of crustal structure using local microearthquakes generated by geothermal activity in Iceland.

In this study, seismic interferometry is applied to recordings of local microseismic events ($M_b < 2$) as energy sources. Unlike true "ambient noise" treatments, in which a wide and quasi-random distribution of a large number of sources at unknown locations is assumed, our approach is to incorporate selected events (microearthquakes) and redatum them in the manner described by *Schuster* [2009] as vertical seismic profiling (VSP) to surface seismic profiling. We will refer here to this imaging technique as Virtual Reflection Seismic Profiling (VRSP). VRSP focuses on using the surface ghost reflection (free-surface multiple) associated with upgoing energy from a subsurface source whose epicenter is relatively near to virtual surface source locations to produce a stacked seismic image comparable to what one would get using real surface sources at those same virtual locations [e.g., *Schuster*, 2009].

2. Study Area

Iceland has long served as perhaps the world's most iconic exposure of mid-ocean ridge processes by virtue of an underlying mantle plume, or hot spot [*Gudmundsson*, 2000]. While much attention was given to the Reykjanes peninsula in southwestern Iceland, where the modern plate boundary comes ashore, volcanic systems throughout Iceland have been of intense scientific and societal concern [e.g., *Gertisser*, 2010]. The Krafla volcanic-geothermal system in particular (Figure 1) has been one of the most studied of the Icelandic magma system due to recurring fissure swarm eruptions over the past centuries [e.g., *Tryggvason*, 1984; *Einarsson*, 1991; *Saemundsson*, 1991; *Harris et al.*, 2000; *Buck et al.*, 2006]. A simple cross-sectional cartoon of the Krafla caldera is shown in Figure 2.

Various seismic measurements have suggested the existence of a magma chamber less than 4 km thick beneath Krafla, with horizontal dimensions of 2 km × 7 km and a top ranging from 3 km to 7 km depth

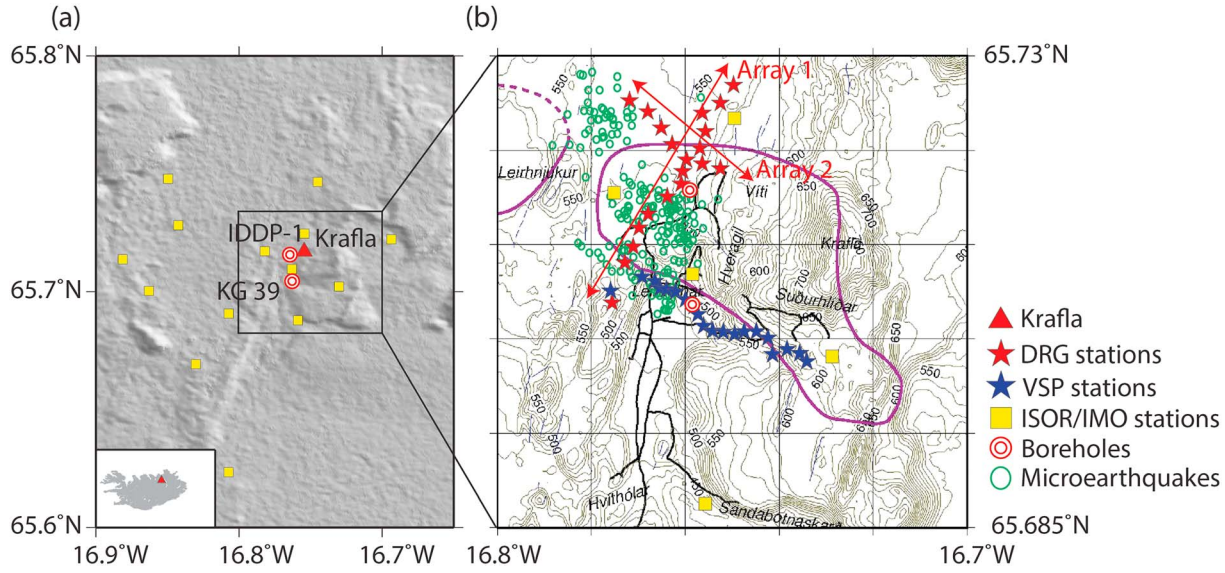

Figure 1. (a) Survey area showing location of IDDP-1 and KG-39 boreholes, the Krafla caldera, and permanent seismic stations (yellow dots). (b) The blue and red stars represent DRG Krafla stations deployed in the recent ISOR/DRG/IMAGE experiment from which the data example in Figure 3 was drawn. Arrays in red are used in this study. The blue stations were deployed for VSP measurements during a recent IMAGE field campaign. Purple contours show estimated boundaries of magma chambers seen as *S* wave shadows during studies of the Krafla Fires (1975–1984) [*Einarsson*, 1978].

[*Einarsson*, 1978; *Brandsdóttir and Menke*, 1992; *Arnott and Foulger*, 1994; *Brandsdóttir et al.*, 1997; *Darbyshire et al.*, 2000]. Recent 3-D tomographic images, generated by inverting both artificial and natural sources, also indicate velocity anomalies that are associated with a magma chamber within the caldera [*Schuler et al.*, 2015].

The magmatic plumbing in Krafla gained particular notoriety in 2009 when a borehole, K-39, unexpectedly encountered magma at depths of 2062 m while drilling into the geothermal system within the central volcano [*Mortensen et al.*, 2010]. Subsequently, the nearby Iceland Deep Drilling Project-1 (IDDP-1) drill hole also drilled into melt at a depth of 2104 m [*Elders et al.*, 2014b]. These magma bodies have received substantial attention both as targets of geochemical and geophysical surveys and as a model for superheated geothermal power generation [*Elders et al.*, 2014a]. The unexpected encounter of rhyolitic magma at such shallow depth also emphasized the limitations of conventional geophysical methods in detecting magma, as these bodies were not recognized in predrilling surveys.

3. Data and Methods

Seismic activity at Krafla is currently monitored by 17 permanent seismic stations (yellow in Figure 1a) operated by ISOR on behalf of the National Power Company and the Iceland Meteorological Office. Krafla was also a subject of recent seismic deployments associated with an ongoing international initiative known as the Integrated Methods for Advanced Geothermal Exploration (IMAGE). The blue stars shown in Figure 1b represent stations deployed for VSP measurements with controlled sources during the IMAGE field campaign [*ISOR*, 2016].

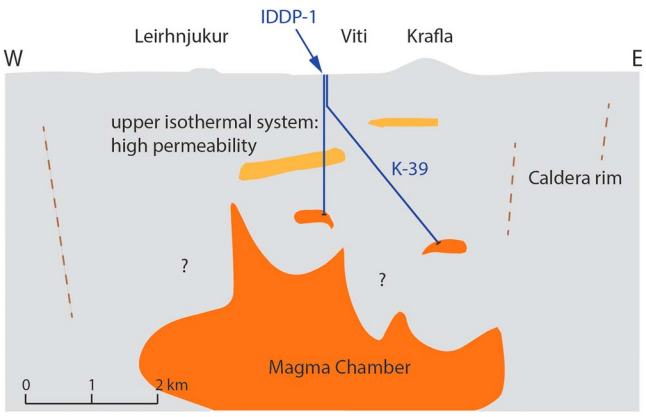

Figure 2. An east-west geologic model for the Krafla caldera. Modified from *Ármannsson et al.* [2014].

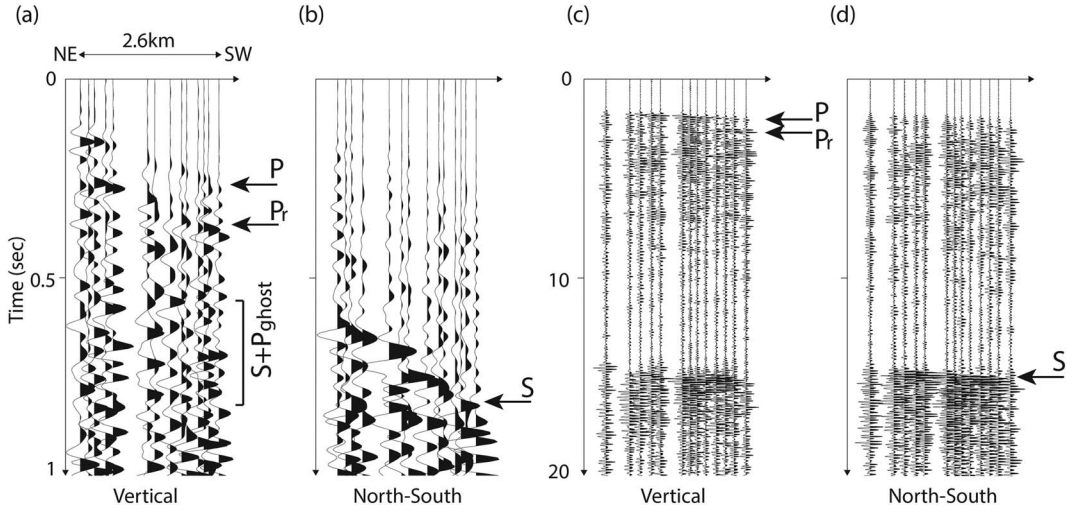

Figure 3. Sample recordings of microearthquakes used in this study. Note: $t = 0$ s time is arbitrary, not the origin time of the earthquake. (a) Vertical component seismogram for earthquake within the seismic array. (b) North-south component of the same local earthquake. (c) Vertical component for an earthquake located at a greater distance, and (d) its north-south component. Traces are depicted for stations extending from northeast to southwest (Array 1 in Figure 1). In addition to clear direct *P* and *S* arrivals, coherent arrivals are evident in the *P* wave coda (e.g., P_r).

As a part of the Deep Roots of Geothermal systems (DRG) project, supported by ISOR, the GEOthermal Research Group (GEORG), and Icelandic power companies, 20 seismic stations were deployed at 200 m spacing as shown by the red stars on Figure 1b. The DRG network used Lennartz 0.2 s sensors with a sampling frequency of 200 Hz. The seismic data were recorded from July to August 2014, and a total of 989 microearthquakes were subsequently detected and located. Figure 3 shows representative recordings of both nearby and relatively distant microearthquakes captured by this array. In addition to prominent direct *P* and *S* arrivals, coherent energy is evident in the *P* wave coda (e.g., P_r in Figure 3). The relatively close spacing between these stations, coupled with the availability of adjacent microearthquake clusters, suggested that the VRSP method might be successful in extracting reflection imagery.

In this study, seismic recordings of 989 microearthquakes of magnitude less than M_2 (smallest M −0.03) were extracted in 1 min windows for imaging beneath Arrays 1 and 2 (Figure 4). We used vertical component records in order to minimize any *S* wave contamination in our *P* wave imaging. The recordings were normalized to the average root mean square amplitude of each window on a trace-by-trace basis for each microearthquake. The strong coherent seismic energy labeled P_r in Figure 3a, arriving shortly after the direct *P* wave, is here interpreted as a reflection of downgoing energy from source reflecting from an interface beneath the hypocenter, an interpretation supported by the analysis described below. To avoid any

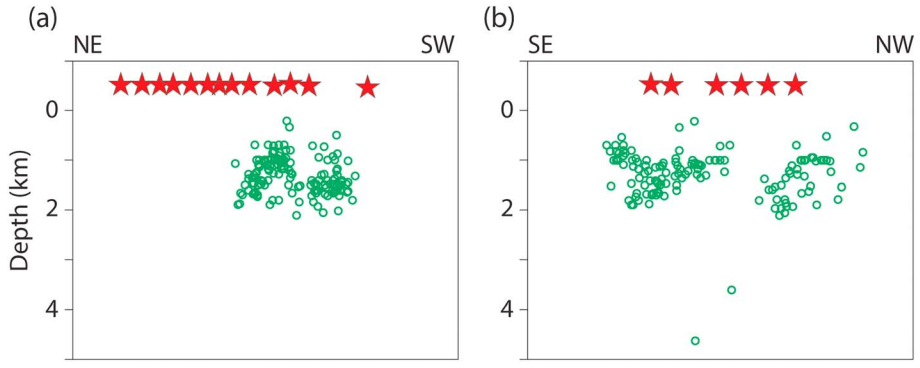

Figure 4. (a) Depth distribution of microearthquakes used in this analysis. Earthquake locations projected onto planes corresponding to the nominal azimuths of Array 1 and (b) Array 2.

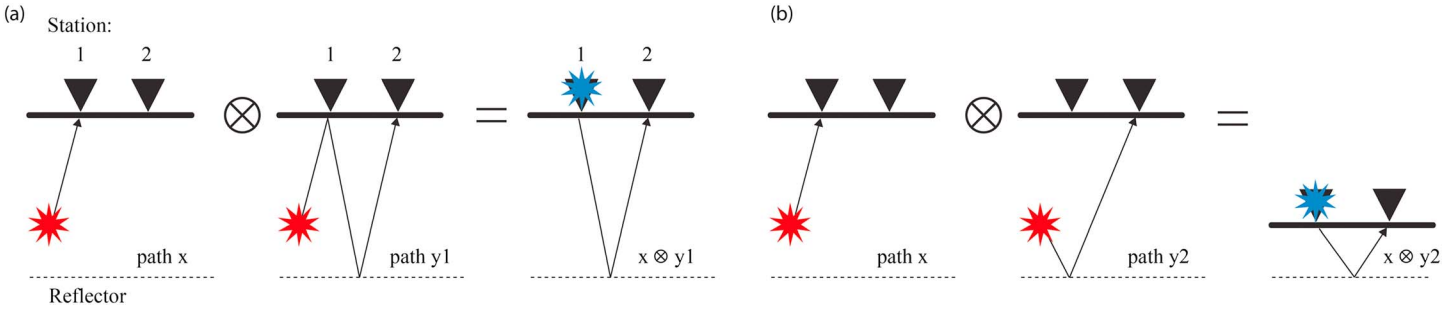

Figure 5. Virtual reflection profiling by redatuming of deep sources. (a) Cross-correlation of the initially upward traveling energy recorded at station 1 with its subsurface reflections recorded by the remaining stations (e.g., station 2) produces a virtual source gather corresponding to a virtual source located at station 1. (b) Cross-correlation of the reflection of the initially downward traveling energy recorded at station 1 with its subsurface reflections recorded by the remaining stations also produces a virtual source gather but one with the sources redatumed to the depth of the real source. After *Schuster* [2009].

individual record dominating summations in which it is involved (e.g., during correlation), these traces were then renormalized on an earthquake ensemble-by-ensemble basis for each individual microearthquake. The recordings were also bandpass filtered with corner frequencies of 2 to 80 Hz prior to cross-correlation in order to emphasize body waves at the expense of any surface wave contributions (e.g., ambient noise). The resulting correlations for each earthquake were then summed to produce either autocorrelations or cross correlations as described below.

The VRSP uses seismic interferometry to redatum the surface-reflected energy (ghost) to surface source positions. This is accomplished by cross-correlating the signals from the station at the virtual source position with those recorded at the remaining real receivers [e.g., *Schuster et al.*, 2004; *Weaver*, 2005; *Torij et al.*, 2007; *Draganov et al.*, 2007]. The basic principle is illustrated in Figure 5a in which correlation of the signals at two stations results in a representation of the signal recorded at one station as if it came from the other station (virtual source). When the offset between virtual source and real receiver is zero, this reproduces the autocorrelation model of *Claerbout* [1968]. In this end-member case, the results are completely independent of the depth or timing of the real event, e.g., microearthquake. If there is a sufficient number and appropriate distribution of sources, then summing all the autocorrelations is equivalent to imaging with ambient noise [e.g., *Draganov et al.*, 2009].

Figure 5b also illustrates how cross-correlation can generate an "artifact" from downgoing energy that encounters a reflecting interface. The result is an apparent reflection occurring at a travel time that corresponds to redatuming of the surface to the depth of the earthquake. Note that this will be only the case for laterally homogeneous medium; however, since in the presence of lateral inhomogeneity, it would not be easy to interpret the resulting artifact as a specific reflection. Although this arrival represents information about the reflection that can be extracted by other methods [e.g., *Quiros et al.*, 2015], it constitutes "noise" in the seismic image keyed to the redatumed ghost (Figure 5a). However, by summing multiple earthquakes from varying depths, the signals corresponding to the raypaths in Figure 5a interfere constructively, while those in Figure 5b tend to interfere destructively [e.g., *Draganov et al.*, 2013].

Another potential artifact that can arise is when the distribution of sources is not uniform with respect to the azimuth. Since VRSP uses the direct waves of the microearthquakes, the directivity of the events may contribute to the result as artifact [e.g., *Emoto et al.*, 2015]. If the *P-S* time interval is sufficiently long to include higher-order multiple reflections from an earthquake, one can process exclusively using coda waves [e.g., *Nishitsuji et al.*, 2016]. Using the *P* wave coda from regional earthquakes for imaging can substantially reduce some artifacts. However, the relatively short *S-P* arrival times relative to the two wave travel times of the ghost reflections of interest for most of the earthquakes in this case (e.g., Figure 3a) preclude effective use of this approach. Moreover, the use of the *P* coda alone depends upon higher-order multiples, which can be expected to be quickly attenuated in a hot volcanic system.

In this study, virtual shot gathers were generated by cross-correlating each station in turn with all the stations for each recorded earthquake, then summing over all microearthquakes. Figure 4 shows the distribution of the microearthquakes selected for imaging projected onto the nominal azimuths of the two recording

arrays. The selection criteria for these events are described in more detail below. However, it is immediately obvious from Figure 4 that the earthquakes are not randomly distributed with respect to the arrays but tend to be asymmetrically clustered in both lateral position and depth. Moreover, the span of these earthquakes would seem to violate one of the conditions of interferometric theory, i.e., that the physical sources should enclose the receivers [*Wapenaar and Fokkema*, 2006; *Draganov et al.*, 2006]. In the following section, we will show how the use of both forward and backward directed virtual shot gathers, together with common reflection point binning of those shot gathers, can overcome these limitations.

After a preliminary analysis of autocorrelation results (see below), seismic reflection sections from the virtual shot gathers were then produced by conventional multichannel processing [e.g., *Yilmaz*, 2001]: common midpoint (CMP) binning (resulting in uniform image spacing), application of normal moveout corrections appropriate for previously measured *P* wave velocities [*Brandsdóttir et al.*, 1997], and then stacking (summing) the recordings for all source-receiver pairs for each CMP bin. To further highlight the dominant reflection signals, the resulting stacks were again bandpass filtered, this time between 6 to 12 Hz. Exponential gain recovery was applied prior to display.

4. Results

4.1. Autocorrelation

Initially, a brute force autocorrelation section was generated by simply adding the autocorrelations of each station's record for all 989 earthquakes (Figures 6a and 6b). This autocorrelation section mimics an unmigrated stacked, single-fold zero source-receiver offset survey. The best results are expected when autocorrelating signals from earthquakes that are either located directly beneath every station or the positions of these sources are well distributed stochastically in space. Thus, we would expect the autocorrelation results to suffer from the clustering of the sources; this should especially be the case for most northeastern stations from Array 1 (Figure 4a). For these "outlier" stations, we would expect virtual reflections to arrive earlier than their real counterparts [*Cabolova*, 2016].

The resulting seismic section for Array 1 (Figure 6a) does exhibit a number of coherent arrivals, both subhorizontal and dipping (e.g., marked by arrows). However, this coherency appears to be relatively localized and scattered, due in part to the irregular spacing between stations. This is especially true for Array 2, which has fewer stations to define coherency. Moreover, the autocorrelations provide little basis for discriminating virtual reflections from coherent artifacts (e.g., Figure 6b). Although the energy in such artifacts can be expected to weaken as the number and depth range of the microearthquake sources increase, the limited number and diversity of events available here may be inadequate for effective mitigation of artifact amplitudes.

4.2. Microearthquakes as Stochastic Noise

The most common approach to extracting body waves from passive recordings is to assume that the source energy arises from unknown but favorably distributed locations [*Draganov et al.*, 2006]. This approach is represented by the stacked reflection section in Figure 7a, computed from virtual shot gathers using all 989 earthquakes recorded by the network. Although the energy binning inherent in the CMP processing results in a more uniform spatial distribution of traces, lateral coherence is still spotty and relatively unconvincing as evidence of subsurface reflectivity. There is a hint of subhorizontal coherency at 0.9 s and a weak but pervasive dipping coherency throughout the section.

Following the methodology of *Nishitsuji et al.* [2016], we have also cross-correlated the *P* coda alone, first using those earthquakes sufficiently distant (i.e. $2° \leq$ epicentral distance $\leq 6°$) to provide an adequate window between *P* and *S* waves (Figure 7b). Before CMP processing of the *P* coda results, the virtual shot gathers were also filtered using multidimensional deconvolution (MDD) using an approximate point spread function (PSF) computed for a time-gate of $|t| < 0.5$ s. This step of applying MDD to interferometry has been found to minimize blurring of the PSF at larger offsets [*Van der Neut et al.*, 2010]. The MDD was performed based on truncated singular-value decomposition. However, the resulting reflection section (Figure 7b) seems to exhibit even less coherency than the autocorrelation and the simple cross-correlation stacks. As mentioned earlier, the higher order multiple reflections upon which this technique is based may be significantly attenuated in this volcanically active and structurally complex area. The seismic section in Figure 7c was produced in the same manner as the section in Figure 7b, but using only local microearthquakes. Although more

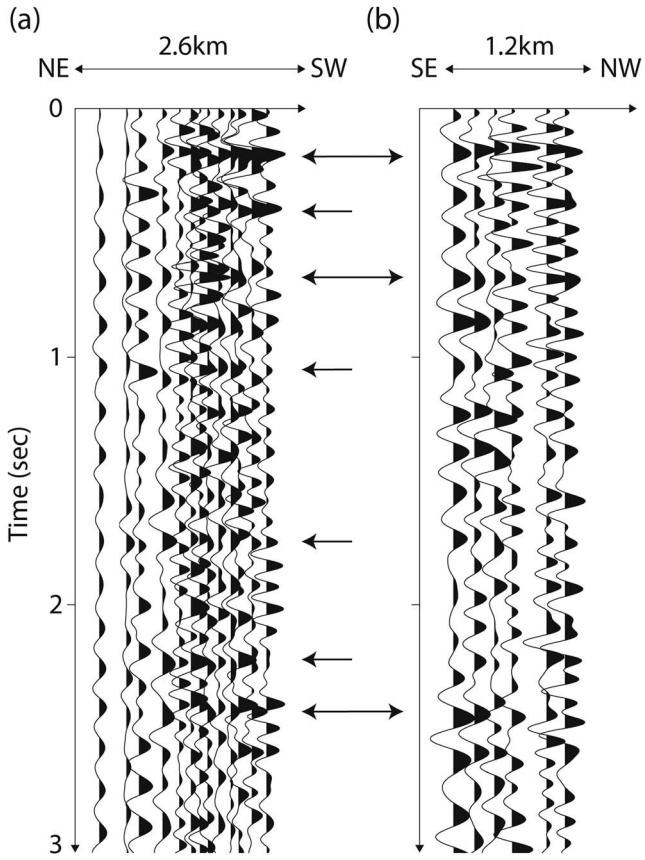

Figure 6. (a) Autocorrelation seismic reflection sections from Array 1 and (b) Array 2. Black arrows indicate coherent phases.

subhorizontal coherency is apparent in Figure 7c versus 7b especially at about 0.8 s, the *P-S* times of the local earthquakes are too short to allow an estimation of the PSF without potential leakage of *S* wave energy into the result.

4.3. Imaging With Selected Earthquakes

There are several possible explanations for the poor results obtained by the ambient noise approach to imaging with the full set (989) of earthquake sources. The issue of attenuation of multiply scattered energy associated with shallow magmatic activity has already been raised. Another possible factor is illustrated in Figure 8. Virtual reflections from offline sources (green circle in Figure 8) sample subsurface locations (blue dots) that are different from the CMP defined by the real stations and both the epicenter of the physical source (gray dots) and the virtual source positions (black dots). This discrepancy will decrease with decreasing offset of the source. The 3-D distribution of earthquake sources results in a lateral spread of subsurface reflection points that sample different reflector positions, thus violating the common reflection point assumption used to bin and stack the data. Therefore, we would expect a better image should result when using only sources which lie beneath and laterally near the recording array so that their virtual CMPs lie within the CMP bins defined by the geometry of the resulting virtual source gathers.

Microearthquakes were thus selected such that their first-order ghost reflection points fall within 100 × 100 m CMP bins defined by the 200 m receiver spacing as shown in Figure 8b. The use of these selected epicenters should (a) minimize lateral offset of virtual reflection points from the CMP bins defined by the virtual source-real receiver geometry as well as (b) minimize the divergence of the normal moveout correction computed from the virtual source-real receiver geometry from the actual moveout displayed by the virtual reflection. The first condition places priority on real sources being near the actual line of receivers. The second condition places a priority on using real sources near the virtual source. [e.g., *Kim et al.*, 2015].

The result of simple cross-correlation and summing of the selected source records is illustrated by the virtual shot gather in Figure 9. It is noticeable that there are clear linear arrivals with apparent velocities (~4.0 km/s) that are consistent with those measured locally for direct *P* waves [*ISOR*, 2016]. Such direct waves imply horizontally propagating energy and near-surface sources; we postulate that this energy is derived from ambient background noise rather than the microearthquakes sensu stricto. More to the point, these virtual shot gathers exhibit more clearly defined coherent phases than the full-blown stacks computed by using the full set of available earthquakes (e.g., Figure 7). Stacked virtual reflection sections produced from virtual shot gathers for selected subsets of the earthquakes are shown in Figures 10 and 11.

It is important to note that the strength of coherent energy (e.g., R2 and R5 in Figures 10 and 11) increases as the number of events used in the stack increases (Figures 10 and 11), supporting our conclusion that they are reflections as opposed to random noise or processing artifacts. However, we found relatively little improvement in the signal to noise as the number of events increased beyond 40. This point of diminishing returns is

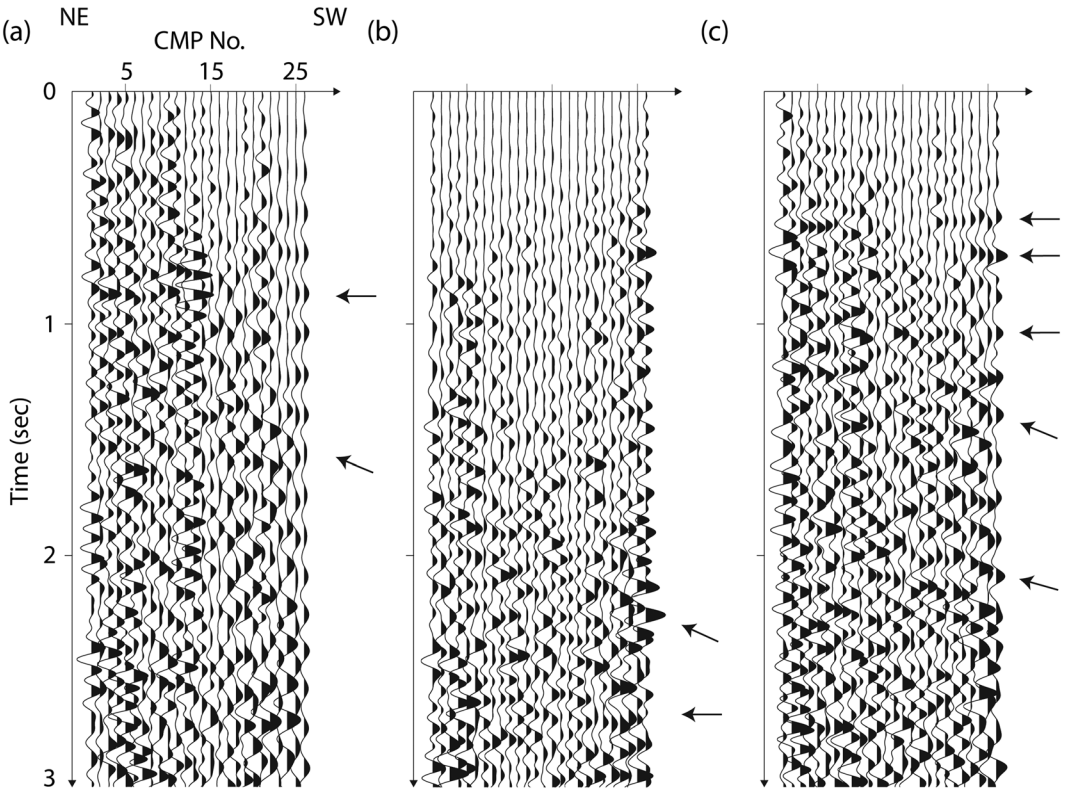

Figure 7. (a) CMP stacked seismic section treating all 989 events as random noise. (b) Stacked section using the *P* wave coda only for 124 selected regional earthquakes. (c) Same as Figure 7b except for the use of 145 local microearthquakes. In both Figures 7b and 7c, MDD was applied after cross-correlation. Arrows indicate coherent phases that may correspond to reflections from physical interfaces at depth.

associated with the inclusion of events that have large offsets from the array, consistent with our expectation that inclusion of more distant sources degrades the stack due to lateral dispersion of the real subsurface reflection points. Whereas all of the events used to produce the section shown in Figures 10a–10d have reflection points that fall within the 100 m × 100 m CMP bins, the additional events in Figure 10e have

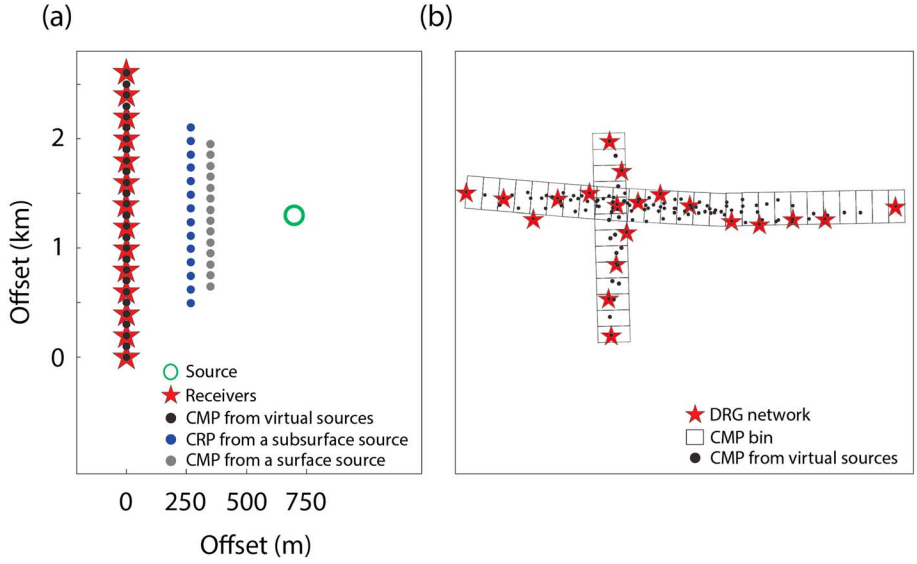

Figure 8. (a) Relative virtual reflection points associated with a source that is laterally displaced from an array. Note the spatial discrepancy between the expected common reflection points (CRP, gray dots) from the conventional common midpoints (CMP, black dots). (b) CMP binning (100 × 100 m) for the DRG arrays.

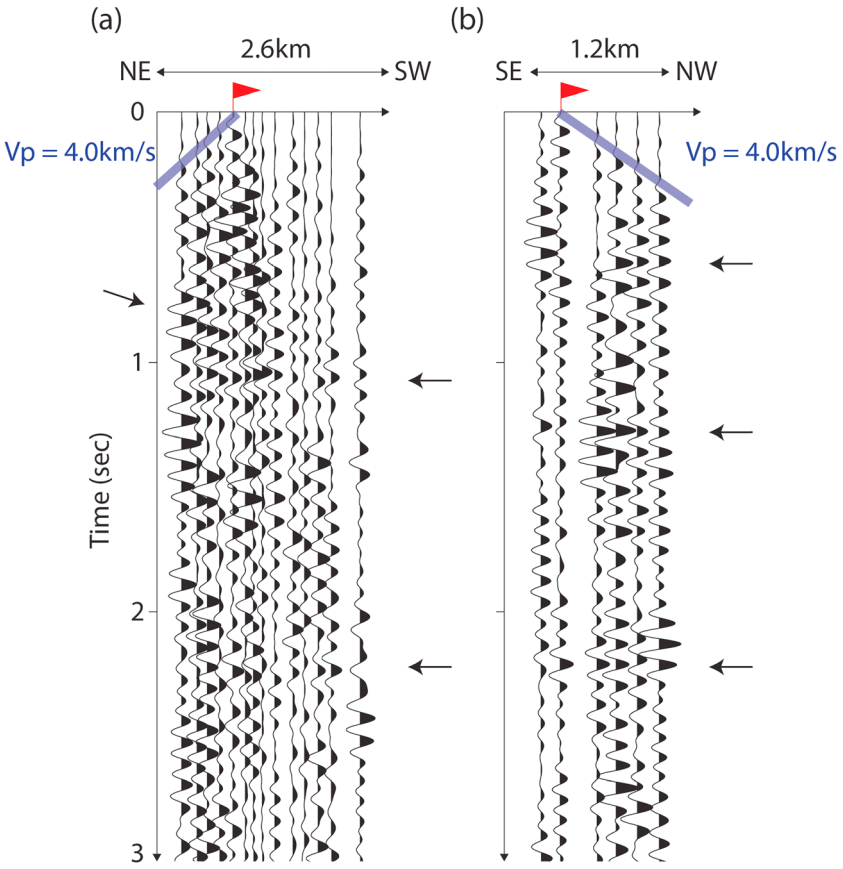

Figure 9. (a) Virtual source gathers for Array 1 and (b) Array 2 computed from selected earthquakes sources. Red flags represent the location of the virtual source. Blue line represents the linear energy, here interpreted as direct virtual *P* wave arrivals and their associated velocity of 4 km/s. Black arrows indicate laterally coherent arrivals interpreted to be reflections from subsurface interfaces.

offsets in excess of 700 m. Note that coherent energy is more evident along Array 1 than Array 2 (Figure 11), which we attribute to the much smaller number of suitably located earthquakes available and smaller number of recording stations along Array 2 (resulting in much lower effective CMP stacking fold). To improve the visibility of reflection energy in these images, a common linear enhancement filter, FX deconvolution [*Yilmaz*, 2001], was applied in Figure 12.

As noted earlier, intrinsic to all of the imaging shown here is the fact that the distribution of earthquakes relative to the station locations would seem to violate the precept in seismic interferometry that the recording stations should be enclosed by the sources. Clearly, for Array 1, for example, the stations at the NE end of the array lie well beyond the selected earthquakes used here. In other words, for these stations, the direct path from earthquake to virtual sources has no commonality with any ghost reflection. Thus, the shot gathers for which these stations are the virtual sources have no useful reflection contribution to make any CMP gather to which they participate. However, this is compensated by the virtual sources to the SW which, with exception of the SW most station, do have an appropriate geometry to generate a virtual reflection at the appropriate time. Thus, almost every CMP gather has a contribution from NE stations as virtual sources and SW stations as virtual sources. The latter is simply the time reverse cross-correlation sum of the former. Thus, each CMP gather has both positive and negative lags of the cross-correlations of each station with another.

5. Discussions

5.1. Interpretation

The features responsible for the more prominent reflection bands in the VRSP (e.g., Figure 13) are largely a matter of conjecture. Since this section does not pass directly over the boreholes (Figure 1b), direct

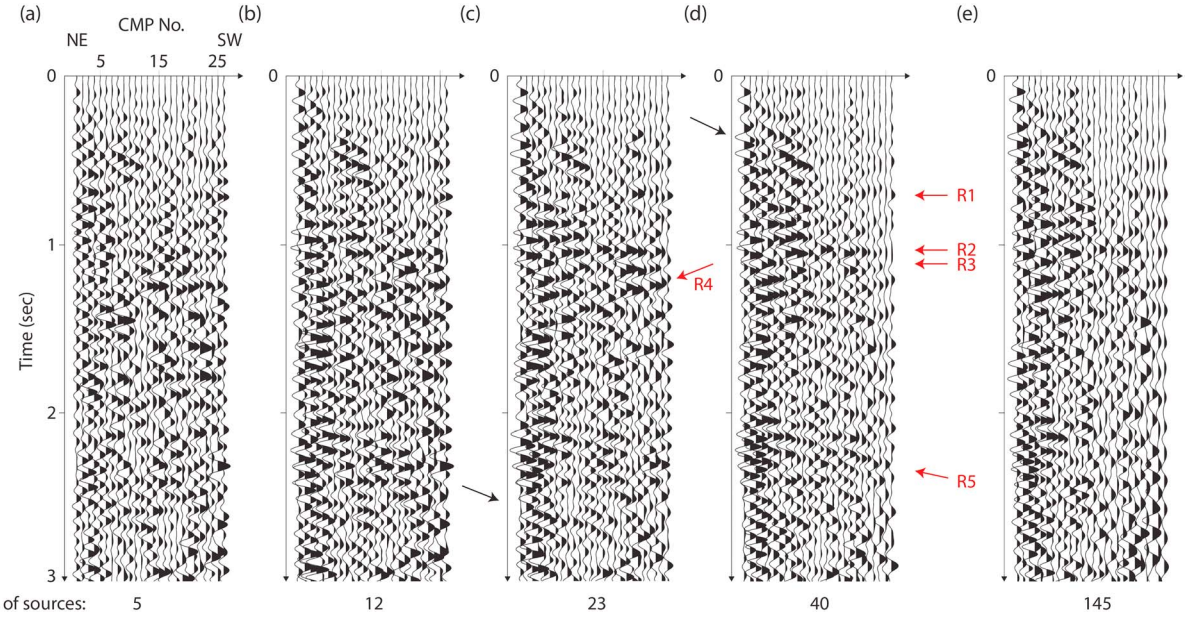

Figure 10. Partial stacks for Array 1 generated with selected earthquake subsets. The number of earthquakes used in each stack, indicated at the bottom of each panel, increases to the right. Increasing CMP no. corresponds to SW direction. R1–R5 indicate coherent reflections discussed in the text. Note R2 corresponds to depth where the magma was drilled. Other coherent phases are also indicated.

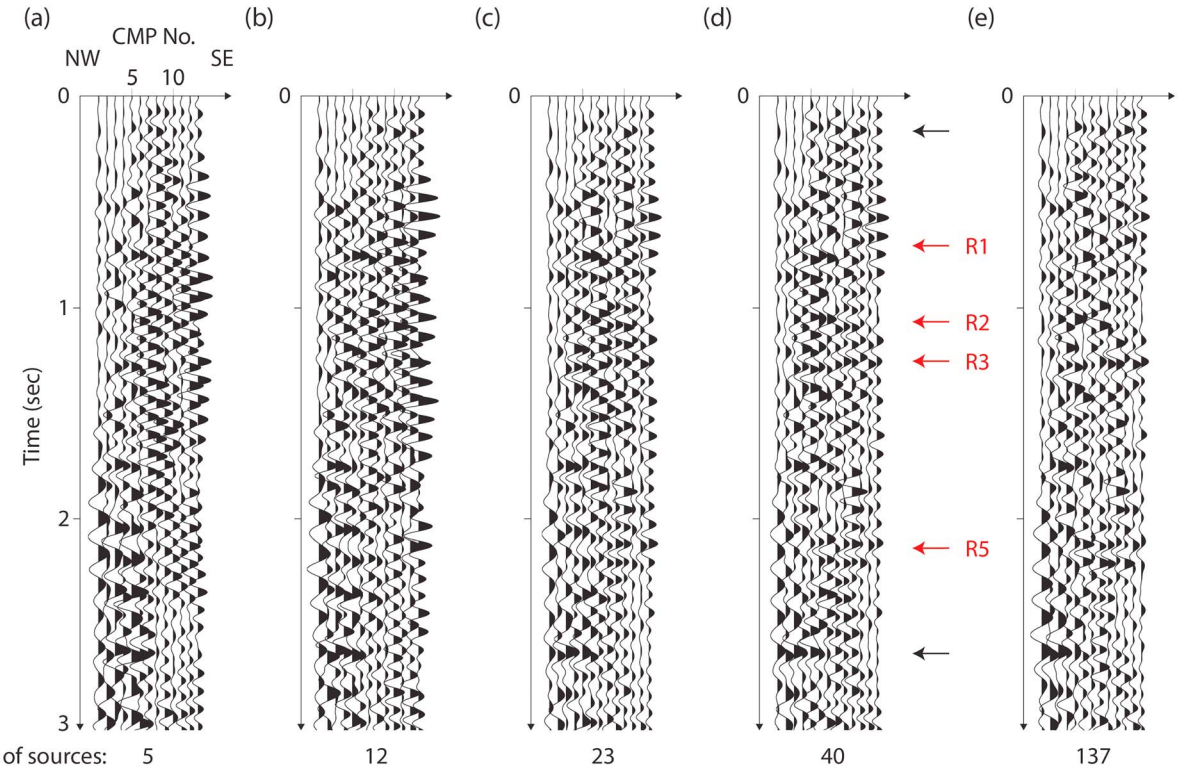

Figure 11. Partial stacked seismic sections for Array 2, generated with selected earthquakes. The number of sources used in each stack, indicated at the bottom of each panel, increases to the right. Increasing CMP no. corresponds to SE direction. R1–R5 are coherent reflections beneath Array 2. Note R2 corresponds to depth where the magma was drilled. Other coherent phases are also indicated.

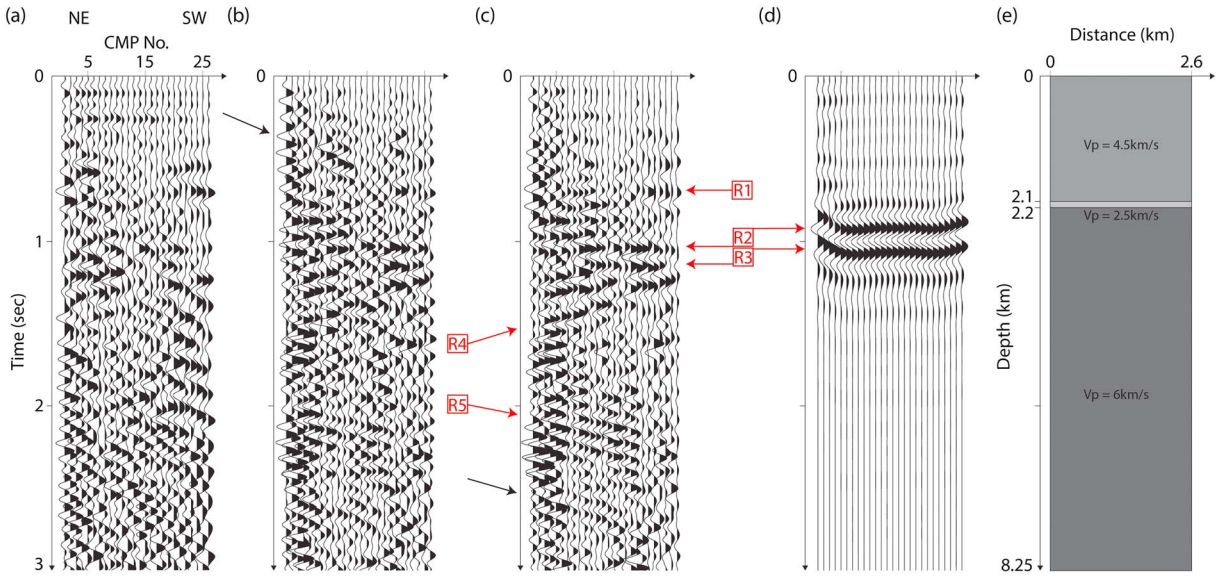

Figure 12. (a) Stacked section of Array1 from Figure 7c enhanced by FX deconvolution. (b) Stacked sections using 23 selected microearthquakes (Figure 8). (c) Stack of selected earthquakes enhanced by FX deconvolution. (d) Simulated VRSP image produced using synthetic virtual source gathers computed from the model in Figure 12e. (e) A simple velocity model of the upper crust at Krafla used to compute the synthetic in Figure 12d. A magma body was placed at a depth comparable to that at which magma was encountered by the Krafla boreholes with an assumed thickness of 100 m. *P* wave velocity (2.5 km/s) for the magma body based on lab measurements [*Murase and Mcbirney*, 1973]. Increasing CMP no. corresponds to the SW direction. The synthetic section was computed using the same geometries of microearthquakes used in Figure 12b. See text for modeling details.

correlations with known lithologic variations are extrapolations at best. However, the prominent phase R2 in Figure 10 corresponds to a depth of about 2.75 km, comparable to the depth of the shallow magma body intersected by IDDP-1 at 2104 km [*Ármannsson et al.*, 2014]. To assess this correlation, a synthetic VRSP (Figure 12c) was computed from the simple geologic model shown in Figure 12d. The thickness of the magma target in the model is arbitrarily set to be 100 m. To obtain the synthetic stack, synthetic seismograms were computed using ray-based modeling software (Omni TM Schlumberger) for 23 impulsive subsurface sources (*P* wave only) with dominant frequencies of 6 to 12 Hz corresponding to the microearthquake distributions used in Figure 12b as they would be recorded by a linear array of 14 receivers at the free surface spaced 200 m apart.

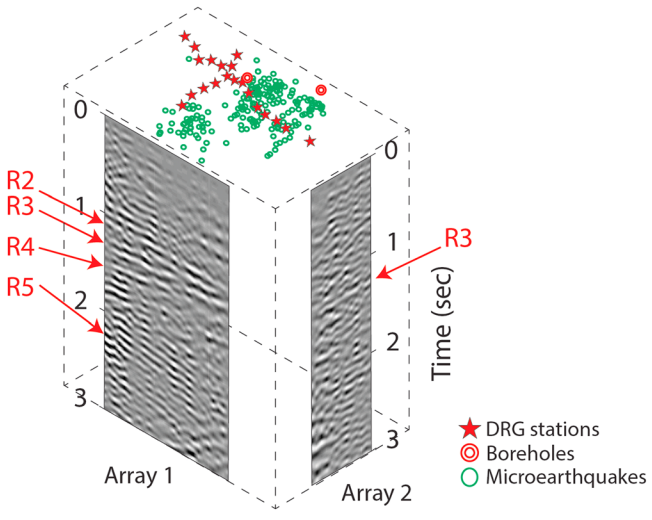

Figure 13. Reflection images of the Krafla subsurface in 3-D fence display. The coherency enhanced reflection images from Array 1 and 2 are displayed here in raster format. The DRG network, microearthquakes source locations, and the two boreholes are also indicated at the top of the figure. R2–R5 are coherent reflections beneath Arrays 1 and 2. R2 corresponds to depth where the magma was encountered in boreholes.

R1 in Figure 12 marks the expected phase that may have resulted from cross-correlating the direct *P* wave with the reflection from the top of the magma reflector of originally downgoing energy from the microearthquake sources, e.g., the geometry depicted in Figure 5b. However, the arrival time on the virtual reflection section for this energy is dependent upon the depth of the source. Hence, stacking such energy for the same reflector but for sources at various depths that illuminates from all angles to the receivers should result in its destruction as a coherent phase [*Draganov et al.*, 2004].

Moreover, no such artifact emerges from the synthetic section (Figure 12c). Finally, this phase is also visible in Figure 7c derived independently using seismic interferometry with coda waves with MDD. Thus, we interpret R1 as most likely a shallow reflector rather than an interferometric artifact.

The flat reflection R2 from the hypothesized magma layer arrives on the synthetic reflection section at the same travel time as the observed phase on the VRSP section derived from the selected microearthquake recordings. This simple correspondence strongly reinforces the association of the coherent subhorizontal phase at about 1 s travel time with the magma encountered during drilling. R2 being a virtual reflection from the magma interface is also consistent with the P_r in Figure 3 being a reflection of the downgoing energy from the same interface (e.g., Figure 5). The cross-correlation of direct *P* arrivals with the ghost reflections from a liquid to solid transition should result in positive polarity reflection, i.e., a deflection to the right (black) on the seismic traces, as is observed on the virtual section. The combination of relatively high amplitude, positive polarity, and flat geometry of R2 are all consistent with a fluid. Although melt is the most likely possibility, due to the correlation to the borehole magma, other fluids associated with magma (entrapped brines, steam, CO_2, SO_2) could also give rise to strong reflection [*Makovsky et al*., 1999]. R3 could correspond to a reflection from its base if it were 500 m thick or simply be another preexisting extrusive or intrusive interface. R4, the dipping band of energy just below R3, is only evident from Array 1; without 3-D control, it could represent energy arriving from out of the plane of the section (e.g., sideswipe).

The identification of other coherent phases is more speculative. R5, for example, could mark the top of the postulated deeper feeder chamber in the geologic model of Krafla (Figure 2) or simply represent another intrusion, lava unit, other fluid (brine, steam) accumulation, or fault. It is important to note that the phases not clearly imaged on the cross line could arise from structure located laterally away from Array 1 (e.g., sideswipe). This ambiguity emphasizes the need for 3-D imaging using a true 2-D surface recording array.

5.2. Complications

Complications not addressed here which could affect VRSP imaging include the following: (a) *S* wave contributions to the cross-correlation functions; (b) variations in microearthquake focal mechanisms, such as polarity changes, that degrade the stack; (c) variations in the source function of rupture, which could likewise negatively affect wavelet stacking; and (d) contributions from converted phases (e.g., *S* to *P*). Although some *S* wave energy may contaminate cross-correlation sums (even though only vertical component records were used here), it should destructively interfere as we increase the number of earthquakes of different *P-S* interval times in the process. Even if such energy still remains in the stack, the direct *P-S* time differences from the selected microearthquakes are too short to explain the magma reflection. Moreover, the velocity used to stack the *P* reflections should work to degrade such arrivals in the CMP stack. The impact of source function variations should be minimal due to the use of small magnitude microearthquakes. Also, the actual wavelet shape is largely irrelevant, as it will be represented by its zero-phase equivalent after correlation. Polarity reversals across focal planes for either the direct or various reflected signals within the array could be detrimental. However, the direct arrivals of the selected microearthquakes exhibit the same polarity across the arrays (e.g., Figure 4) suggesting polarity changes due to focal mechanisms are not a serious issue.

6. Conclusions

The K-39 and the IDDP-1 wells provide a unique opportunity for calibrating geophysical methods against a known magma target at depth. In this study, we show how body waves from microearthquakes can be processed by seismic interferometry (VRSP) to produce high-resolution reflection imageries beneath the geothermal field at Krafla, Iceland. The VRSP image produced by the pilot dataset contains prominent reflections that correspond to the depth of a magma body encountered by the IDDP-1 well. Other virtual reflections could correspond to additional intrusions, including feeder chambers, buried extrusive layering, or even fluid pockets. However, true 3-D recording (e.g., 2-D dense surface array) is needed to properly position many of these features; thus, their identification at present is speculative at best. Dense recording arrays, such as those used in this study, represent a new capability to generate high-resolution subsurface imagery. Such technology is becoming more economically available even for 2-D arrays for true 3-D imaging in the form of the continuously recording nodal systems now in common use in oil exploration [e.g., *Lin et al*., 2013b; *Inbal et al*., 2015]. We do not suggest that VRSP is a replacement for more conventional, controlled source survey at the surface. However, it does have the obvious advantage of not requiring the use of expensive artificial

sources, such as explosives in boreholes or vibroseis trucks. It also eliminates any negative environmental or societal impacts, not to mention acquisition permit difficulties, associated with artificial sources at the surface. The cost differential becomes particularly acute if time-lapse imaging (i.e., multiple surveys to search for time-dependent changes in reflectivity at depth) is desired. The advantage of this approach over teleseismic techniques (e.g., receiver functions) is the higher resolution that can be achieved from the higher frequency content of microseismic events. Ambiguities notwithstanding these results confirm virtual reflection techniques as a promising new method for detecting and mapping subsurface structure at sites characterized by high levels of microseismicity.

Acknowledgments

We would like to acknowledge our appreciation to ISOR, GEORG, and the National Power Company in Iceland for providing the data and Schlumberger for providing seismic analysis software (VISTA 3D and Omni 3D). ISOR acknowledges Olafur Gudmundsson and Ari Tryggvason at Uppsala University who played an instrumental role in the planning and designing of the field experiment in Krafla. ISOR also thanks Karin Berglund at Uppsala University and Palmar Sigudsson at ISOR for their dedication to the fieldwork. The authors are particularly appreciative of the many helpful suggestions from Deyan Draganov in his review of earlier drafts of this work. In this study, Doyeon Kim was supported by an NSF grant (grant 966045) as a part of Integrative Graduate Education and Research Traineeship (IGERT) program at Cornell University. The data for this paper are available by contacting the corresponding author at dk696@cornell.edu.

References

Ármannsson, H., T. Fridriksson, G. H. Gudfinnsson, M. Ólafsson, F. Óskarsson, and D. Thorbjörnsson (2014), IDDP—The chemistry of the IDDP-01 well fluids in relation to the geochemistry of the Krafla geothermal system, *Geothermics*, *49*, 66–75.

Arnott, S. K., and G. R. Foulger (1994), The Krafla spreading segment, Iceland: 1. Three-dimensional crustal structure and the spatial and temporal distribution of local earthquakes, *J. Geophys. Res.*, *99*, 23,801–23,825.

Benz, H. M., and R. B. Smith (1984), Simultaneous inversion for lateral velocity variations and hypocenters in the Yellowstone region using earthquake and refraction data, *J. Geophys. Res.*, *89*, 1208–1220.

Brandsdóttir, B., and W. H. Menke (1992), Thin low-velocity zone within the Krafla caldera, NE-Iceland attributed to a small magma chamber, *Geophys. Res. Lett.*, *19*, 2381–2384.

Brandsdóttir, B., W. Menke, P. Einarsson, R. S. White, and R. K. Staples (1997), Färoe-Iceland Ridge Experiment 2. Crustal structure of the Krafla central volcano, *J. Geophys. Res.*, *102*, 7867–7886.

Brocher, T. M. (1981), Geometry and physical properties of the Socorro, New Mexico, magma bodies, *J. Geophys. Res.*, *86*, 9420–9432.

Brown, L. D., P. A. Krumhansl, C. E. Chapin, A. R. Sanford, F. A. Cook, S. Kaufman, J. E. Oliver, and F. S. Schilt (1979), COCORP seismic reflection studies of the Rio Grande rift, in *Rio Grande Rift: Tectonics and Magmatism*, edited by R. E. Riecker, pp. 169–184, AGU, Washington, D. C., doi:10.1029/SP014p0169.

Brown, L. D., W. Zhao, K. D. Nelson, M. Hauck, D. Alsdorf, A. Ross, M. Cogan, M. Clark, X. Liu, and J. Che (1996), Bright spots, structure, and magmatism in southern Tibet from INDEPTH seismic reflection profiling, *Science*, *274*(5293), 1688–1690.

Buck, W. R., P. Einarsson, and B. Brandsdóttir (2006), Tectonic stress and magma chamber size as controls on dike propagation: Constraints from the 1975–1984 Krafla rifting episode, *J. Geophys. Res.*, *111*, B12404, doi:10.1029/2005JB003879.

Cabolova, A. (2016), Seismic investigation of deep 2D, 3D and 4D structures using body wave interferometry, computer simulations and semi-conventional processing, PhD thesis, Cornell Univ.

Cassidy, J. F. (1992), Numerical experiments in broadband receiver function analysis, *Bull. Seismol. Soc. Am.*, *82*(3), 1453–1474.

Claerbout, J. F. (1968), Synthesis of a layered medium from its acoustic transmission response, *Geophysics*, *33*(2), 264–269.

Corry, C. E. (1988), *Laccoliths: Mechanics of Emplacement and Growth*, vol. 220, Geol. Soc. of Am., Boulder, Colo.

Crisp, J. A. (1984), Rates of magma emplacement and volcanic output, *J. Volcanol. Geotherm. Res.*, *20*, 177–211.

Darbyshire, F. A., K. F. Priestley, R. S. White, R. Stefánsson, G. B. Gudmundsson, and S. S. Jakobsdóttir (2000), Crustal structure of central and northern Iceland from analysis of teleseismic receiver functions, *Geophys. J. Int.*, *143*(1), 163–184.

Draganov, D., K. Wapenaar, and J. Thorbecke (2004), Passive seismic imaging in the presence of white noise sources, *Lead. Edge*, *23*(9), 889–892.

Draganov, D., K. Wapenaar, and J. Thorbecke (2006), Seismic interferometry: Reconstructing the Earth's reflection response, *Geophysics*, *71*(4), SI61–SI70.

Draganov, D., K. Wapenaar, W. Mulder, J. Singer, and A. Verdel (2007), Retrieval of reflections from seismic background-noise measurements, *Geophys. Res. Lett.*, *34*, L04305, doi:10.1029/2006GL028735.

Draganov, D., X. Campman, J. Thorbecke, A. Verdel, and K. Wapenaar (2009), Reflection images from ambient seismic noise, *Geophysics*, *74*(5), A63–A67.

Draganov, D., X. Campman, J. Thorbecke, A. Verdel, and K. Wapenaar (2013), Seismic exploration-scale velocities and structure from ambient seismic noise (> 1 Hz), *J. Geophys. Res. Solid Earth*, *118*, 4345–4360, doi:10.1002/jgrb.50339.

Einarsson, P. (1978), *S*-wave shadows in the Krafla caldera in NE-Iceland, evidence for a magma chamber in the crust, *Bull. Volcanol.*, *41*(3), 187–195.

Einarsson, P. (1991), The Krafla rifting episode 1975–1989, in *Náttúra Mývatns, (Nature of Lake Mývatn)*, edited by A. Gardarsson and A. Einarsson, pp. 97–139, Icelandic Nature Science Society, Reykjavik.

Elders, W. A., G. Friḥleifsson, and A. Albertsson (2014a), Drilling into magma and the implications of the Iceland Deep Drilling Project (IDDP) for high-temperature geothermal systems worldwide, *Geothermics*, *49*, 111–118.

Elders, W. A., G. Ó. Friḥleifsson, and B. Pálsson (2014b), Iceland Deep Drilling Project: The first well, IDDP-1, drilled into magma, *Geothermics*, (*49*), 1.

Emerman, S. H., and R. Marrett (1990), Why dikes?, *Geology*, *18*(3), 231–233.

Emoto, K., M. Campillo, F. Brenguier, X. Briand, and T. Takeda (2015), Asymmetry of coda cross-correlation function: Dependence of the epicentre location, *Geophys. J. Int.*, *201*(3), 1313–1323.

Gertisser, R. (2010), Eyjafjallajökull volcano causes widespread disruption to European air traffic, *Geol. Today*, *26*(3), 94–95.

Glazner, A. F., and W. Ussler (1988), Trapping of magma at midcrustal density discontinuities, *Geophys. Res. Lett.*, *15*, 673–675.

Gorbatov, A., E. Saygin, and B. L. N. Kennett (2013), Crustal properties from seismic station autocorrelograms, *Geophys. J. Int.*, *192*(2), 861–870.

Gudmundsson, A. (2000), Dynamics of volcanic systems in Iceland: Example of tectonism and volcanism at juxtaposed hot spot and mid-ocean ridge systems, *Annu. Rev. Earth Planet. Sci.*, *28*(1), 107–140.

Harris, A. J. L., J. B. Murray, S. E. Aries, M. A. Davies, L. P. Flynn, M. J. Wooster, R. Wright, and D. A. Rothery (2000), Effusion rate trends at Etna and Krafla and their implications for eruptive mechanisms, *J. Volcanol. Geotherm. Res.*, *102*(3), 237–269.

Huang, H.-H., F.-C. Lin, B. Schmandt, J. Farrell, R. B. Smith, and V. C. Tsai (2015), The Yellowstone magmatic system from the mantle plume to the upper crust, *Science*, *348*(6236), 773–776.

Inbal, A., R. W. Clayton, and J.-P. Ampuero (2015), Imaging widespread seismicity at midlower crustal depths beneath Long Beach, CA, with a dense seismic array: Evidence for a depth-dependent earthquake size distribution, *Geophys. Res. Lett.*, *42*, 6314–6323, doi:10.1002/2015GL064942.

Ishihara, K. (1990), Pressure sources and induced ground deformation associated with explosive eruptions at an andesitic volcano: Sakurajima volcano, Japan, in *Magma Transport and Storage*, edited by M. P. Ryan, pp. 335–356, John Wiley, New York.
ISOR (2016), Active seismic with VSP in Krafla, NE-Iceland, IMAGE – Summary report of Task 4.2.
Iyer, H. M., J. R. Evans, G. Zandt, R. M. Stewart, J. M. Coakley, and J. N. Roloff (1981), A deep low-velocity body under the Yellowstone caldera, Wyoming: Deviation using teleseismic *P*-wave residuals and tectonic interpretation, *Geol. Soc. Am. Bull.*, *92*(11 Part II), 1471–1646.
Kennett, B. L. N. (2015), Lithosphere–asthenosphere *P*-wave reflectivity across Australia, *Earth Planet. Sci. Lett.*, *431*, 225–235.
Kent, G. M., et al. (2000), Evidence from three-dimensional seismic reflectivity images for enhanced melt supply beneath mid-ocean-ridge discontinuities, *Nature*, *406*(6796), 614–618.
Kim, D., L. D. Brown, D. Quiros (2015), Body wave imaging with interferometry of aftershock sources, in 2015 SEG Annual Meeting, Society of Exploration Geophysicists.
Lees, J. M. (2007), Seismic tomography of magmatic systems, *J. Volcanol. Geotherm. Res.*, *167*(1), 37–56.
Lin, F.-C., M. P. Moschetti, and M. H. Ritzwoller (2008), Surface wave tomography of the western United States from ambient seismic noise: Rayleigh and Love wave phase velocity maps, *Geophys. J. Int.*, *173*(1), 281–298.
Lin, F.-C., V. C. Tsai, B. Schmandt, Z. Duputel, and Z. Zhan (2013a), Extracting seismic core phases with array interferometry, *Geophys. Res. Lett.*, *40*, 1049–1053, doi:10.1002/grl.50237.
Lin, F.-C., D. Li, R. W. Clayton, and D. Hollis (2013b), High-resolution 3D shallow crustal structure in Long Beach, California: Application of ambient noise tomography on a dense seismic array, *Geophysics*, *78*(4), Q45–Q56.
Makovsky, Y., S. L. Klemperer, L. Ratschbacher, and D. Alsdorf (1999), Midcrustal reflector on INDEPTH wide-angle profiles: An ophiolitic slab beneath the India-Asia suture in southern Tibet?, *Tectonics*, *18*(5), 793–808, doi:10.1029/1999TC900022.
Matsumoto, S., and A. Hasegawa (1996), Distinct *S* wave reflector in the midcrust beneath Nikko-Shirane volcano in the northeastern Japan arc, *J. Geophys. Res.*, *101*, 3067–3083.
Mortensen, A. K., K. Grönvold, A. Guḥmundsson, B. Steingrímsson, and T. Egilson (2010), Quenched silicic glass from well K-39 in Krafla, north-eastern Iceland, in Proceedings World Geothermal Congress, Bali, Indonesia.
Murase, T., and A. R. Mcbirney (1973), Properties of some common igneous rocks and their melts at high temperatures, *Geol. Soc. Am. Bull.*, *84*(11), 3563–3592.
Mutter, J. C., G. A. Barth, P. Buhl, R. S. Detrick, J. Orcutt, and A. Harding (1988), Magma distribution across ridge-axis discontinuities on the East Pacific Rise from multichannel seismic images, *Nature*, *336*(6195), 156–158, doi:10.1038/336156a0.
Nakata, N., R. Snieder, and M. Behm (2014), Body-wave interferometry using regional earthquakes with multidimensional deconvolution after wavefield decomposition at free surface, *Geophys. J. Int.*, *199*(2), 1125–1137.
Nelson, K. D. et al. (1996), Partially molten middle crust beneath southern Tibet: Synthesis of project INDEPTH results, *Science*, *274*(5293), 1684–1688.
Nishitsuji, Y., S. Minato, B. Boullenger, M. Gomez, K. Wapenaar, and D. Draganov (2016), Crustal-scale reflection imaging and interpretation by passive seismic interferometry using local earthquakes, *Interpretation*, SJ29–SJ53.
Parsons, T., N. H. Sleep, and G. A. Thompson (1992), Host rock rheology controls on the emplacement of tabular intrusions: Implications for underplating of extending crust, *Tectonics*, *11*(6), 1348–1356.
Polteau, S., A. Mazzini, O. Galland, S. Planke, and A. Malthe-Sørenssen (2008), Saucer-shaped intrusions: Occurrences, emplacement and implications, *Earth Planet. Sci. Lett.*, *266*(1), 195–204.
Quiros, D., L. D. Brown, A. Cabolova, C. Chen, K. Davenport, J. Hole, L. Han, M. C. Chapman, and W. Mooney (2015), Reflection imaging using earthquake sources: A novel application of reverse vertical seismic profiling (RVSP), in 2015 SEG Annual Meeting, Society of Exploration Geophysicists.
Roux, P., K. G. Sabra, P. Gerstoft, W. A. Kuperman, and M. C. Fehler (2005), *P*-waves from cross-correlation of seismic noise, *Geophys. Res. Lett.*, *32*, L19303, doi:10.1029/2005GL023803.
Ruigrok, E., and K. Wapenaar (2012), Global-phase seismic interferometry unveils *P*-wave reflectivity below the Himalayas and Tibet, *Geophys. Res. Lett.*, *39*, L11303, doi:10.1029/2012GL051672.
Ryberg, T. (2011), Body wave observations from cross-correlations of ambient seismic noise: A case study from the Karoo, RSA, *Geophys. Res. Lett.*, *38*, L13311, doi:10.1029/2011GL047665.
Saemundsson, K. (1991), Geology of the Krafla system, in *The Natural History of Lake Myvatn*, edited by A. Gardarsson and P. Einarsson, pp. 24–95, The Icelandic Natural History Society, Reykjavik.
Sanford, A. R., and L. T. Long (1965), Microearthquake crustal reflections, Socorro, New Mexico, *Bull. Seismol. Soc. Am.*, *55*(3), 579–586.
Sanford, A. R., Ö. Alptekin, and T. R. Toppozada (1973), Use of reflection phases on microearthquake seismograms to map an unusual discontinuity beneath the Rio Grande rift, *Bull. Seismol. Soc. Am.*, *63*(6–1), 2021–2034.
Sanford, A. R., R. P. Mott, P. J. Shuleski, E. J. Rinehart, F. J. Caravella, R. M. Ward, and T. C. Wallace (1977), Geophysical evidence for a magma body in the crust in the vicinity of Socorro, New Mexico, in *The Earth's Crust*, *Geophys. Monogr. Ser*, vol. 20, edited by J. G. Heacock, pp. 385–403, AGU, Washington, D. C.
Scarpa, R. (2001), Predicting volcanic eruptions, *Science*, *293*(5530), 615–616.
Schuler, J., T. Greenfield, R. S. White, S. W. Roecker, B. Brandsdóttir, J. M. Stock, J. Tarasewicz, H. R. Martens, and D. Pugh (2015), Seismic imaging of the shallow crust beneath the Krafla central volcano, NE Iceland, *J. Geophys. Res. Solid Earth*, *120*, 7156–7173, doi:10.1002/2015JB012350.
Schuster, G. T., J. Yu, J. Sheng, and J. Rickett (2004), Interferometric/daylight seismic imaging, *Geophys. J. Int.*, *157*(2), 838–852.
Schuster, G. T. (2009), *Seismic Interferometry*, pp. 1–274, Cambridge Univ. Press, Cambridge.
Shapiro, N. M., M. Campillo, L. Stehly, and M. H. Ritzwoller (2005), High-resolution surface-wave tomography from ambient seismic noise, *Science*, *307*(5715), 1615–1618.
Sheetz, K. E., and J. W. Schlue (1992), Inferences for the Socorro magma body from teleseismic receiver functions, *Geophys. Res. Lett.*, *19*, 1867–1870.
Spera, F. J. (1980), Aspects of magma transport, in *Physics of Magmatic Processes*, edited by R. B. Hargraves, pp. 265–315, Princeton Univ. Press, Princeton, N. J.
Tibuleac, I. M., and D. von Seggern (2012), Crust-mantle boundary reflectors in Nevada from ambient seismic noise autocorrelations, *Geophys. J. Int.*, *189*(1), 493–500.
Torij, K., et al. (2007), Application seismic interferometry to natural earthquakes measured by small-scale array, in SEG Technical Program Expanded Abstracts 2007, pp. 1362–1366, Society of Exploration Geophysicists.
Tryggvason, E. (1984), Widening of the Krafla fissure swarm during the 1975–1981 volcano-tectonic episode, *Bull. Volcanol.*, *47*(1), 47–69.
Van der Neut, J., E. Ruigrok, D. Draganov, and K. Wapenaar (2010), Retrieving the Earth's reflection response by multi-dimensional deconvolution of ambient seismic noise, in 72nd EAGE Conference and Exhibition incorporating SPE EUROPEC 2010.

Voight, B., and R. R. Cornelius (1991), Prospects for eruption prediction in near real-time, *Nature*, *350*(6320), 695–698.
de Voogd, B., L. Serpa, L. Brown, E. Hauser, S. Kaufman, J. Oliver, B. W. Troxel, J. Willemin, and L. A. Wright (1986), Death Valley bright spot: A midcrustal magma body in the southern Great Basin, California?, *Geology*, *14*(1), 64–67.
Wapenaar, K., and J. Fokkema (2006), Green's function representations for seismic interferometry, *Geophysics*, *71*(4), SI33–SI46.
Wapenaar, K., J. van der Neut, and E. Ruigrok (2008), Passive seismic interferometry by multidimensional deconvolution, *Geophysics*, *73*(6), A51–A56.
Ward, K. M., G. Zandt, S. L. Beck, D. H. Christensen, and H. McFarlin (2014), Seismic imaging of the magmatic underpinnings beneath the Altiplano-Puna volcanic complex from the joint inversion of surface wave dispersion and receiver functions, *Earth Planet. Sci. Lett.*, *404*, 43–53.
Weaver, R. L. (2005), Information from seismic noise, *Science*, *307*(5715), 1568–1569, doi:10.1126/science.1109834.
Wei, W. et al. (2001), Detection of widespread fluids in the Tibetan crust by magnetotelluric studies, *Science*, *292*(5517), 716–719.
Yilmaz, Ö. (2001), *Seismic Data Analysis*, pp. 159–270, Society of Exploration Geophysicists, Tulsa, Okla.
Yu, J., and G. T. Schuster (2001), Crosscorrelogram migration of IVSPWD data, in SEG Technical Program Expanded Abstracts 2001, pp. 456–459, Society of Exploration Geophysicists.
Zandt, G., M. Leidig, J. Chmielowski, D. Baumont, and X. Yuan (2003), Seismic detection and characterization of the Altiplano-Puna magma body, central Andes, *Pure Appl. Geophys.*, *160*(3–4), 789–807.
Ziolkowski, A., P. Hanssen, R. Gatliff, H. Jakubowicz, A. Dobson, G. Hampson, X.-Y. Li, and E. Liu (2003), Use of low frequencies for sub-basalt imaging, *Geophys. Prospect.*, *51*(3), 169–182.